

# High-Strain-Rate Material Behavior and Adiabatic Material Instability in Impact of Micron-Scale Al-6061 Particles

Qiyong Chen<sup>1</sup> · Arash Alizadeh<sup>1</sup> · Wanting Xie<sup>2,3</sup> · Xuemei Wang<sup>4</sup> · Victor Champagne<sup>5</sup> · Andrew Gouldstone<sup>1</sup> · Jae-Hwang Lee<sup>2</sup> · Sinan Müftü<sup>1</sup>

Submitted: 23 October 2017 / in revised form: 5 January 2018  
© ASM International 2018

**Abstract** Impact of spherical particles onto a flat sapphire surface was investigated in 50–950 m/s impact speed range experimentally and theoretically. Material parameters of the bilinear Johnson–Cook model were determined based on comparison of deformed particle shapes from experiment and simulation. Effects of high-strain-rate plastic flow, heat generation due to plasticity, material damage, interfacial friction and heat transfer were modeled. Four distinct regions were identified inside the particle by analyzing temporal variation of material flow. A relatively small volume of material near the impact zone becomes unstable due to plasticity-induced heating, accompanied by severe drop in the flow stress for impact velocity that exceeds  $\sim 500$  m/s. Outside of this region, flow stress is reduced due to temperature effects without the instability. Load carrying capacity of the material degrades and the material expands horizontally leading to jetting. The increase in overall plastic and frictional dissipation with impact velocity was found to be inherently lower than the increase in the kinetic energy at high speeds, leading to the instability. This work introduces a novel method to

characterize HSR ( $10^9 \text{ s}^{-1}$ ) material properties and also explains coupling between HSR material behavior and mechanics that lead to extreme deformation.

**Keywords** adiabatic shear instability · Al-6061 · cold spray · high strain rate · Johnson–Cook model · material instability · particle impact

## List of symbols

$A$	Static yield stress, MPa
$A_c$	Contact area, $\text{m}^2$
$B$	Coefficient of strain hardening, MPa
$c$	Specific heat, J/kg K
$C$	Bilinear strain rate coefficient
$D1$	Height of deformed particle, m
$D2$	Diameter of deformed particle, m
$D_p$	Diameter of particle, m
$e$	Coefficient of restitution
$E$	Elastic modulus, error between experiment and simulation aspect ratios
$E_k$	Kinetic energy of particle, J
$E_r$	Recovered strain energy, J
$k$	Thermal conductivity, W/m K
$m$	Index of thermal softening
$m_p$	Mass of particle, kg
$n$	Index of strain-rate hardening
$R_e$	Experimental aspect ratio
$R_s$	Simulated aspect ratio
$T$	Temperature, K
$T^*$	Homologous temperature
$T_m$	Melting temperature, K
$T_R$	Reference temperature, K
$U_p$	Energy dissipated due to plastic action, J
$v_i$	Impact velocity, m/s
$v_r$	Rebound velocity, m/s

✉ Sinan Müftü  
s.muftu@neu.edu

<sup>1</sup> Department of Mechanical and Industrial Engineering, Northeastern University, Boston, MA 02115, USA

<sup>2</sup> Department of Mechanical and Industrial Engineering, University of Massachusetts, Amherst, MA 01002, USA

<sup>3</sup> Department of Physics, University of Massachusetts, Amherst, MA 01002, USA

<sup>4</sup> United Technologies Research Center, East Hartford, CT 06108, USA

<sup>5</sup> United States Army Research Laboratory, Aberdeen Proving Ground, Aberdeen, MD 21005, USA

$W_f$  Work done against friction, J  
 $\mathbf{x}$  Optimization variable vector

### Greek letters

$\alpha$  Thermal expansion ratio,  $K^{-1}$   
 $\beta$  Inelastic heat fraction  
 $\varepsilon_f$  Failure shear strain  
 $\varepsilon_p$  Equivalent plastic strain  
 $\dot{\varepsilon}_0$  Reference strain rate,  $s^{-1}$   
 $\dot{\varepsilon}_c$  Critical reference strain rate,  $s^{-1}$   
 $\dot{\varepsilon}_p$  Equivalent plastic strain rate,  $s^{-1}$   
 $\mu$  Kinetic friction coefficient  
 $\nu$  Poisson's ratio  
 $\rho$  Mass density,  $kg/m^3$   
 $\sigma_Y$  Yield (flow) stress, MPa

### Subscripts

$r$  Material properties at room temperature

### Acronyms

CS Cold spray  
 FEA Finite element analysis  
 GZ Gao-Zhang  
 HSR High strain rate  
 JC Johnson–Cook  
 KHL Khan–Huang–Liang  
 LIPIT Laser-induced projectile impact test  
 PDMS Polydimethylsiloxane  
 PTW Preston–Tonk–Wallace  
 VA Voyiadjis–Abed  
 ZA Zerilli–Armstrong

## Introduction

Cold particle gas spray, or cold spray (CS), is an additive manufacturing technology which allows solid-state deposition of coatings and three-dimensional manufacturing of free form objects by using a metal and mixture of metal and ceramic powders. In this technology, micron-scale particles accelerate in a supersonic gas stream to velocities in the range of 400–1200 m/s (Ref 1). The resulting impact lasts 20–40 ns and causes the strain rates to reach  $10^8 s^{-1}$  where extreme physics of the material would be expected (Ref 2). Deformation mechanics of the particle is significantly affected by the changes in the flow stress due to the strain and strain-rate hardening and the thermal softening caused by excessive plastic action in the material. Experimental techniques such as the Split-Hopkinson pressure/tension bar tests (SHPB/SHTB) (Ref 3–7) and the Split-Hopkinson shear bar tests (Ref 8–11) are able to characterize the high-strain-rate material behavior for strain rates up to  $10^4 s^{-1}$ , and the theoretical aspects of HSR material behavior have

been investigated by many investigators (Ref 12–18). The fundamental mechanisms involved in bonding of micron-scale particles following high-velocity impacts are still not thoroughly understood. Several hypotheses have been proposed, among which the most popular are: (i) solid/liquid-state atomic diffusion across the contact interface (Ref 19, 20), (ii) material mixing (Ref 21) and interfacial instability-induced mechanical interlocking/roll-ups (Ref 22–24) and (iii) metallic adhesion under high pressure (Ref 19, 25–30). The interface energy for bonded particles was shown to be close to the grain boundary energy (Ref 31–33).

Grujicic et al. (Ref 19) reported that the contribution from the atomic-level inter-diffusion to bonding is likely to be small, considering the duration and the dimensions of the impact. They indicate metallic adhesion assisted by adiabatic shear instability near or on the contact interface to be the dominant bonding mechanism in the absence of mechanical interlocking. Severe interface shear is thought to clean the surfaces from oxides and other impurities exposing clean metal that can form some type of adhesion (Ref 19). Champagne et al. (Ref 21) reported that adiabatic shear instability also promotes material mixing between copper particle and aluminum substrate. Bonding due to localized material melting and mechanical interlocking at the interface as a result of adiabatic shear instability has also been studied (Ref 24, 34–36). Wright et al. (Ref 37–40) carried out a series of fundamental investigation on the theory of adiabatic shear instability and localization. Based on their works, Grujicic et al. (Ref 19) developed a one-dimensional model to predict the onset velocity of adiabatic shear localization and showed good correlation with experiment and finite element analysis (FEA) results (Ref 19, 25). The two-dimensional axisymmetric geometry with Lagrangian formulation, however, tends to overestimate the deformation in the jetting region. Models that include material failure have been considered in order to represent the interface mechanics more realistically (Ref 41).

Xie et al. (Ref 42) conducted experiments that involve impact of micron-scale Al-6061 particles with a sapphire surface in room temperature by using a unique experimental technique that allows the control of impact velocities in the range of 50–950 m/s. A HSR material model was calibrated based on the experimental results and continuum simulations. In the present work, detailed analysis of the HSR effects on material behavior and on deformation mechanics is presented.

## Laser-Induced Single Particle Impact Experiments

*Laser-induced projectile impact test* (LIPIT), an experimental technique that could accelerate micron-scale powders to supersonic velocity, was used in this work (Ref

43, 44). The combined experimental and theoretical work shows that the strain rates can reach  $10^9 \text{ s}^{-1}$  at the high end of the velocity range (950 m/s) in impact of Al-6061 with a sapphire surface (Ref 42). Barradas et al. (Ref 45) introduced laser shock cladding of micron-scale metal plates which showed the possibility of controllably accelerating individual particles to high velocities. Later, impact of a micron-scale particle onto substrates using similar laser shock technology was reported (Ref 46–48). In this work, particles are placed on a PDMS/Au/glass substrate. One single particle is aimed at a time and accelerated toward a sapphire substrate by the rapidly expanding PDMS film, upon laser ( $\lambda = 1,064 \text{ nm}$ ) ablation of the Au film. Ultra-fast imaging via  $\sim 100 \text{ fs}$  light pulses ( $\lambda = 740 \text{ nm}$ ) enables the recording of particle in flight. With this method, Al particles can be accelerated to velocities well over 1 km/s. The velocity of a particle is measured by capturing its positions using the multiple exposure photography, as seen in Fig. 1. The individual exposures correspond to consecutive probe pulses with a defined time interval (for example, 302 ns in Fig. 1). Deceleration of the particle due to air drag is negligible.

As one of the goals of this work is to calibrate the material plasticity model for Al-6061 in the high-strain-rate (HSR) regime, sapphire was chosen as the substrate material. With the significantly higher stiffness of sapphire

than that of aluminum, complex substrate effects are excluded from the analysis of HSR behavior of the particle. The diameter of each particle was measured using an optical microscope prior to the LIPIT experiment. The particle diameters ranged from 14 to 25  $\mu\text{m}$ . A total of 63 impacts were performed and corresponding impact and rebound velocities were determined as described above. To study the postmortem morphologies, several rebound particles were captured and characterized by scanning electron microscope (SEM). The impact velocities in these experiments varied in the range of 50–950 m/s.

## Finite Element Simulations

The impact of a spherical, micron-scale Al-6061 with a flat sapphire substrate was simulated by using the commercially available finite element analysis (FEA) software package ABAQUS/Explicit 6.13-2 (Ref 49). The explicit time integration scheme (Ref 31, 49–51) was adopted due to the highly complex and nonlinear interactions between contact, large deformation and plasticity that occurs during the impact process. The duration of simulation was set to 100 ns in order to ensure that the particle rebound is fully captured in analysis. The effects of gravitational force were ignored in this work.

A quarter symmetric model (Fig. 2) was used in order to reduce the computational cost, by taking into account the axisymmetric nature of the geometry. The outer and bottom boundaries of the substrate were fixed, and symmetry boundary conditions were applied on the two lateral, flat

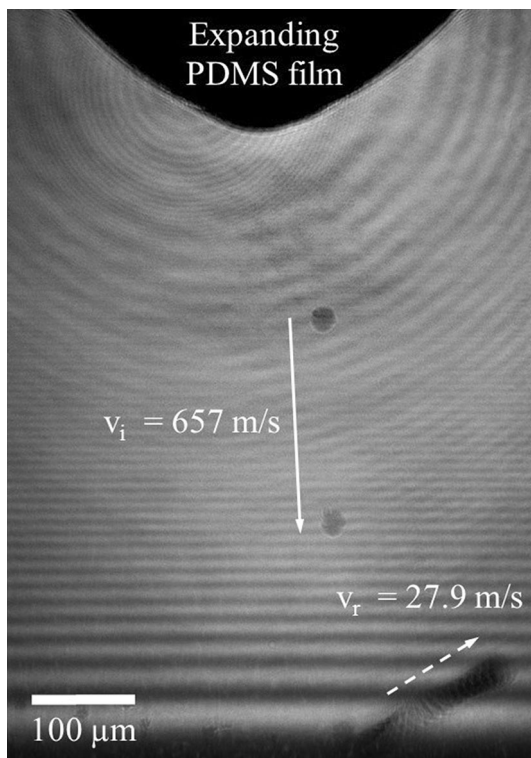


**Fig. 1** The collision and rebound of an Al-6061 particle with the sapphire substrate is captured by multiple exposure photography

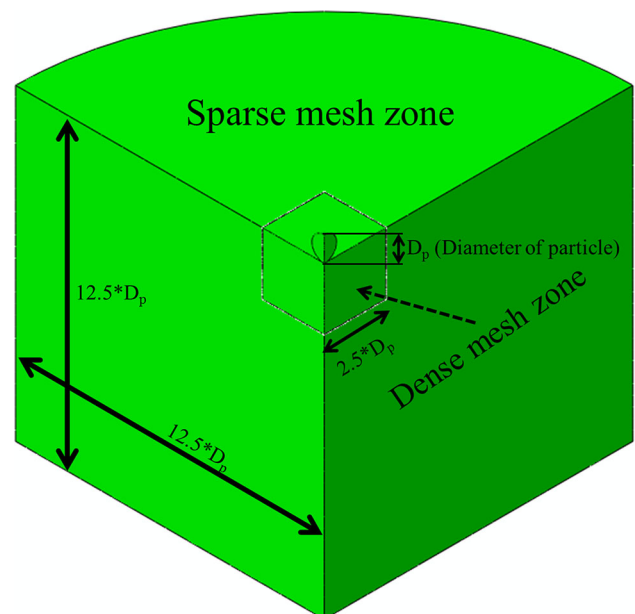


**Fig. 2** Geometry of the axisymmetric model

surfaces shown in Fig. 2. The substrate was partitioned to two zones: a central *dense mesh region* where the impact takes place and a surrounding *sparse mesh region* where extreme material behavior is not expected. The two distinct mesh zones of the substrate were connected by the mesh tie constraints which make all the degrees of freedom from both sides of the interface conform to each other throughout the entire simulation. The height and radius of the substrate were both 12.5 times of the particle diameter, whereas the central region was in a cubic shape with its side length being 2.5 times of the particle diameter. These parameters were examined to ensure that the waves reflecting from the boundaries will not interfere with the contact and rebound behavior (Ref 25). A series of mesh convergence tests showed that a reasonable element size for the particle in the dense mesh region is  $D_p/25$ . In the sparse mesh region, the element size was chosen roughly 10 times larger than that of the dense mesh region.

The general contact algorithm was used for modeling the contact and the interaction between the particle and the substrate. For the normal behavior, hard contact was specified as a pressure–overclosure relationship, which minimizes the penetration of the particle surface into the substrate surface. In the tangential direction, the classic Coulomb friction model was employed where the interface can transmit shear stresses up to a certain magnitude before the two contacting surfaces start sliding with respect to each other. It was assumed that the friction coefficient is identical in all directions. Heat can be generated from kinetic friction of contacting surfaces, and the energy is evenly distributed between the two contacting bodies. Heat can also be generated due to plastic action in the material. In this work, it was assumed that 90% of the plastic strain energy turns into heat. Therefore, the *inelastic heat fraction*  $\beta$  was set to 0.9. This effect serves as an internal heat source in the model. Initial temperatures of the substrate and the particle were set to the initial temperature of the experiments (293 K). The element type used for all bodies in this simulation was C3D8RT (Ref 49) which is a first-order, 3D continuum element with eight nodes and a single integration point. To tackle the excessive unrealistic element distortion that comes with reduced integration, enhanced hourglass control (Ref 52) was adopted. This element allows coupled simulation of displacements and temperature effects on the continuum, and the heat conduction.

Material properties of Al-6061 and sapphire, reported in Table 1 and Fig. 3, were taken from the MPDB material database (Ref 53) and the literature (Ref 54–56). The material properties of Al-6061 depend on temperature as shown in Fig. 3, with reference temperatures provided in Table 1 (Ref 50). Note that variation of the mass density of Al-6061 with temperature, and the temperature effects on

**Table 1** Material properties

<i>Particle (Al-6061)</i>	
$E_r$ , Elastic modulus, GPa	69.11
$\rho$ , Mass density, kg/m <sup>3</sup>	2700
$\nu_r$ , Poisson's ratio	0.331
$\alpha_r$ , Thermal expansion ratio, K <sup>-1</sup>	$2.23 \times 10^{-5}$
$k_r$ , Thermal conductivity, W/m K	154
$c_r$ , Specific heat, J/kg K	1009
$\beta$ , Inelastic heat fraction	0.9
$T_m$ , Melting temperature, K	925
$T_R$ , Reference temperature, K	293
$\varepsilon_f$ , Failure shear strain	3
$\mu$ , Kinetic friction coefficient	0.3
<i>Substrate (sapphire)</i>	
$E$ , Elastic modulus, GPa	345
$\rho$ , Mass density, kg/m <sup>3</sup>	3980
$\nu$ , Poisson's ratio	0.29
$\alpha$ , Thermal expansion ratio, K <sup>-1</sup>	$6.98 \times 10^{-6}$
$k$ , Thermal conductivity, W/m K	23
$c$ , Specific heat, J/kg K	896

Subscript “r” in the particle section refers to room temperature, and the corresponding property is temperature dependent. All other quantities without subscript are constant

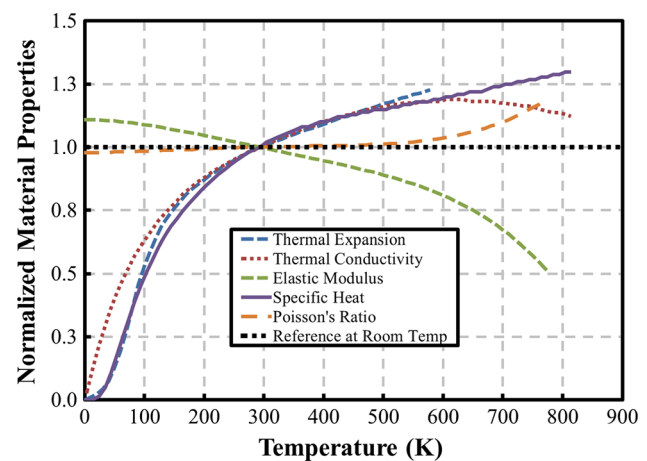


**Fig. 3** Temperature-dependent material properties of Al-6061, normalized with respect to room temperature values

sapphire material properties were not considered in this work.

Also, due to the large deformation involved, it is necessary to describe the progressive damage and failure for the material; therefore, element deletion (Ref 57, 58) was adopted. The criterion for damage initiation is met when  $w = \sum \Delta \varepsilon_p / \varepsilon_f = 1$  (Ref 41), where  $\Delta \varepsilon_p$  is an increment of the equivalent plastic strain,  $\varepsilon_f$  is the failure shear strain. The damage parameter  $w$  increases monotonically as



plastic deformation progresses during impact. After damage initiation, the load carrying capacity of the material degrades progressively.

### Material Model for High-Strain-Rate Plastic Deformation

Mechanics of this high deformation impact problem is dominated by the plastic flow of the material. There are numerous material models for high-strain-rate material deformation including the models by Johnson and Cook (JC) (Ref 14, 59), Zerilli and Armstrong (ZA) (Ref 12, 60), Voyiadjis and Abed (VA) (Ref 18), Preston–Tonk–Wallace (PTW) (Ref 17), Khan–Huang–Liang (KHL) (Ref 15, 16, 61) and Gao and Zhang (GZ) (Ref 13). In general, these models involve numerous material constants that need to be determined empirically. Rahmati et al. compared all six material models above in simulations of the cold spray process (Ref 62). They showed that the jetting phenomenon commonly observed in cold spray experiments was predicted with JC and PTW models. They reported that VA, the modified KHL and ZA models did not predict the flow stress over a wide range of strains and strain rates, whereas the GZ model overestimated the flow stress for copper and was unable to predict the critical velocity of particle bonding with substrate. The JC model involves fewer material constants than the PTW model, with abundant material constants reported in the literature for many materials. However, this model underestimates the flow stress at very high strain rates. Manes et al. reported that the JC model underestimates the flow stress for strain rates that are greater than  $1000 \text{ s}^{-1}$  for Al-6061 (Ref 54, 55). Their work shows that experimental data on flow stress can be represented well by using a bilinear strain rate coefficient  $C$ . The bilinear JC flow stress model was presented in the following form,

$$\sigma_Y = \left( A + B \varepsilon_p^n \right) \left( 1 + C \ln \frac{\dot{\varepsilon}_p}{\dot{\varepsilon}_0} \right) \left( 1 - \left( \frac{T - T_R}{T_m - T_R} \right)^m \right),$$

$$\text{with } C = \begin{cases} C_1 & \text{and } \dot{\varepsilon}_0 = 1 & \text{if } \dot{\varepsilon}_p < \dot{\varepsilon}_c \\ C_2 & \text{and } \dot{\varepsilon}_0 = \dot{\varepsilon}_c & \text{if } \dot{\varepsilon}_p > \dot{\varepsilon}_c \end{cases} \quad (\text{Eq 1})$$

where  $\sigma_Y$  is the flow stress,  $A$ ,  $B$ ,  $C$ ,  $n$  and  $m$  are the empirically determined material parameters,  $\varepsilon_p$  is the equivalent plastic strain,  $\dot{\varepsilon}_p$  is the equivalent strain rate,  $\dot{\varepsilon}_0$  is the reference strain rate,  $T_m$  is the melting temperature of the material and  $T_R$  is the reference temperature. The three terms in brackets represent the effects of strain hardening, strain-rate hardening and thermal softening, respectively. In particular, the coefficient  $C$  and the reference strain rate  $\dot{\varepsilon}_0$  control the strain-rate hardening behavior. Experiments

show that the flow stress,  $\sigma_Y$ , increases drastically with logarithmic strain rate,  $\ln(\dot{\varepsilon}_p/\dot{\varepsilon}_0)$ , above a critical strain rate  $\dot{\varepsilon}_c$ . Lesuer et al. (Ref 63) attributed the change in the strain rate coefficient to two internal, sequential processes: the cutting or bypassing of obstacles by dislocations; and the drag on moving dislocations by phonons or electrons. In other words, different rates represent the deformation mechanisms associated with discrete obstacles or drag. The bilinear form of the JC model, therefore, involves two constants,  $C_1$  and  $C_2$ , and the critical reference strain rate,  $\dot{\varepsilon}_c$ . A user subroutine (UMAT) that reflects the bilinear strain rate coefficient,  $C$ , behavior was prepared using Abaqus/Explicit simulations of impact.

### Material Parameters for the Bilinear JC Model

Figure 4 shows the particle profiles measured from the SEM images of the deformed particles for 180, 290, 420, 530, 660 and 700 m/s impact speeds. The *experimental aspect ratio* of the deformed particles  $R_e$ , defined as shown in Fig. 4a, was assessed from the experiments. The *simulated aspect ratio*,  $R_s$ , was determined from the simulation results. The error  $E$  between the measured and simulated aspect ratio was defined as follows (Ref 50),

$$E(x) = \frac{(R_e - R_s)^2}{R_e^2} \times 100 \quad (\text{Eq 2})$$

The error is a function of the optimization variable vector  $x = \{A, B, C_1, C_2, m, n, \dot{\varepsilon}_c\}$  which contains the six parameters of the bilinear JC plasticity model (Ref 50). The vector  $x$  which minimizes the error for a given impact velocity was found iteratively, by using a modified form of the method of the steepest descent (Ref 64, 65). The optimized material properties for each case are presented in Table 2. The deformed shapes and simulation results are compared in Fig. 4. Simulation results show very good match with the experiments in terms of post-impact particle shape.

### Material Instability During Impact Process

#### Rebound Behavior

In general, the rebound behavior of a particle can be summarized in the *coefficient of restitution*,  $e$ , which is commonly defined as the square root of the ratio between the non-rotational kinetic energies of rebound and impact,  $\sqrt{m_p v_r^2 / m_p v_i^2}$ . The coefficient of restitution can also be represented as  $e = v_r / v_i$  without loss of generality, in case no material is lost during impact. Figure 5a shows the

**Fig. 4** Comparison of postmortem particle morphologies from experiment and simulation. Simulation results with deformed particle shapes measured from SEM images by using MATLAB's Image Processing Toolbox.

(a)  $v_i = 175$  m/s,  $D_p = 18.95$   $\mu\text{m}$ , (b)  $v_i = 286$  m/s,  $D_p = 22.60$   $\mu\text{m}$ , (c)  $v_i = 416$  m/s,  $D_p = 22.50$   $\mu\text{m}$ , (d)  $v_i = 530$  m/s,  $D_p = 20.90$   $\mu\text{m}$ , (e)  $v_i = 663$  m/s,  $D_p = 17.95$   $\mu\text{m}$ , (f)  $v_i = 699$  m/s,  $D_p = 21.60$   $\mu\text{m}$

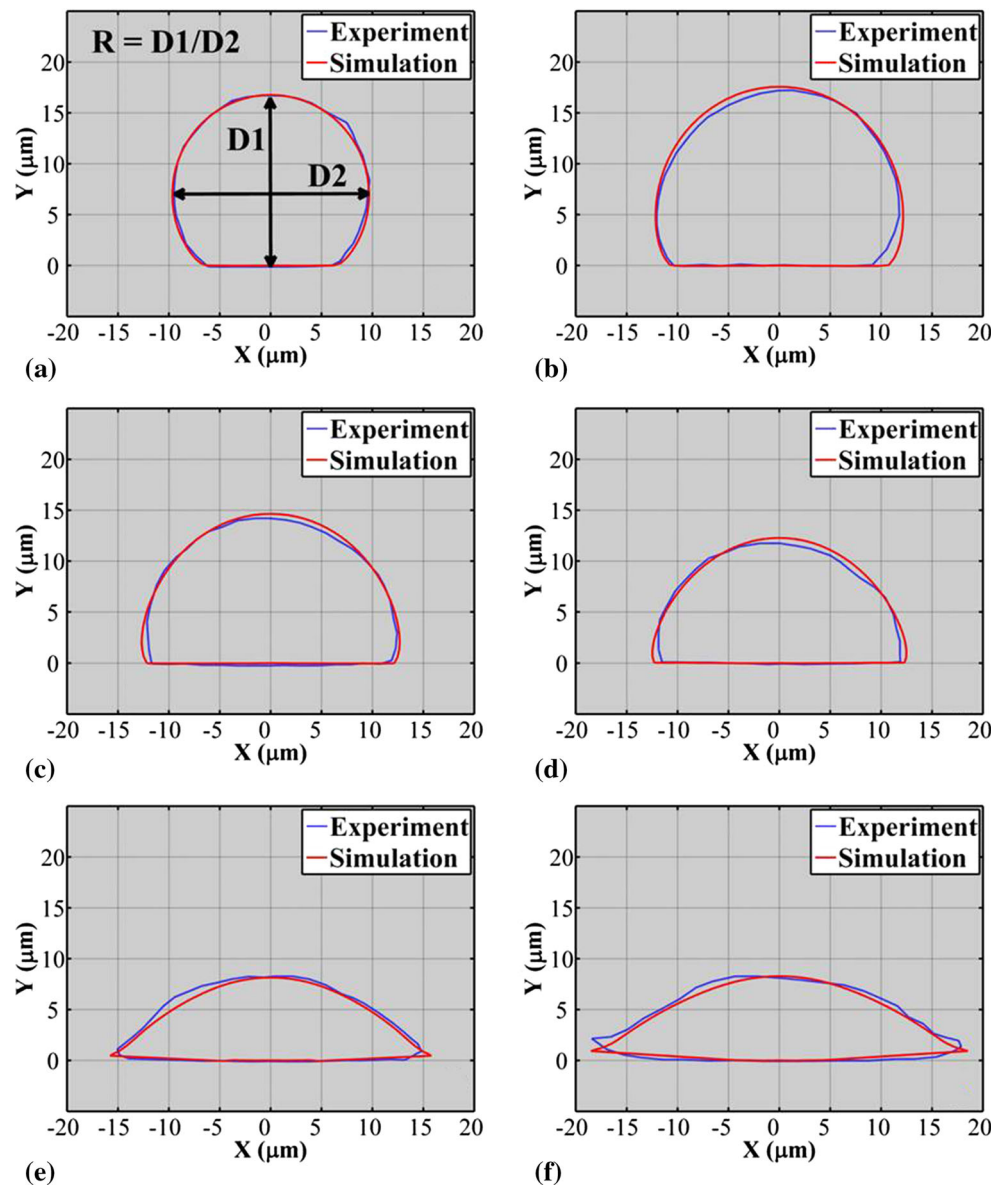


**Table 2** Experiment parameters and optimized bilinear JC parameters

Case #	$D_p$ , $\mu\text{m}$	$V_i$ , m/s	$A$	$B$	$C_1$	$C_2$	$m$	$n$	$\dot{\epsilon}_c$
Initial values (Ref 54)			270	154.3	0.002	0.1301	1.34	0.2215	597.2
1	18.95	175	270	154.3	0.002	0.027	1.74	0.2215	597.2
2	22.60	286	270	154.3	0.002	0.011	1.44	0.2215	597.2
3	22.50	416	270	154.3	0.002	0.027	1.34	0.2400	597.2
4	20.90	530	270	154.3	0.002	0.055	1.34	0.2215	597.2
5	17.95	663	270	154.3	0.002	0.027	1.34	0.2600	597.2
6	21.60	699	270	154.3	0.002	0.027	1.34	0.2700	597.2
Average			270	154.3	0.002	0.029	1.42	0.239	597.2

measured and computed values of the coefficient of restitution as a function of impact velocity for the micron-scale Al-6061 particles impacting the sapphire surface. Note that particle size does not have a significant effect on the

coefficient of restitution as a function of impact velocity. This is expected as coefficient of restitution is a function of parameter  $v_i^2/2\sigma_Y$  (Ref 66, 67). In fact, Fig. 6 shows that the post-impact particle profiles are independent of particle

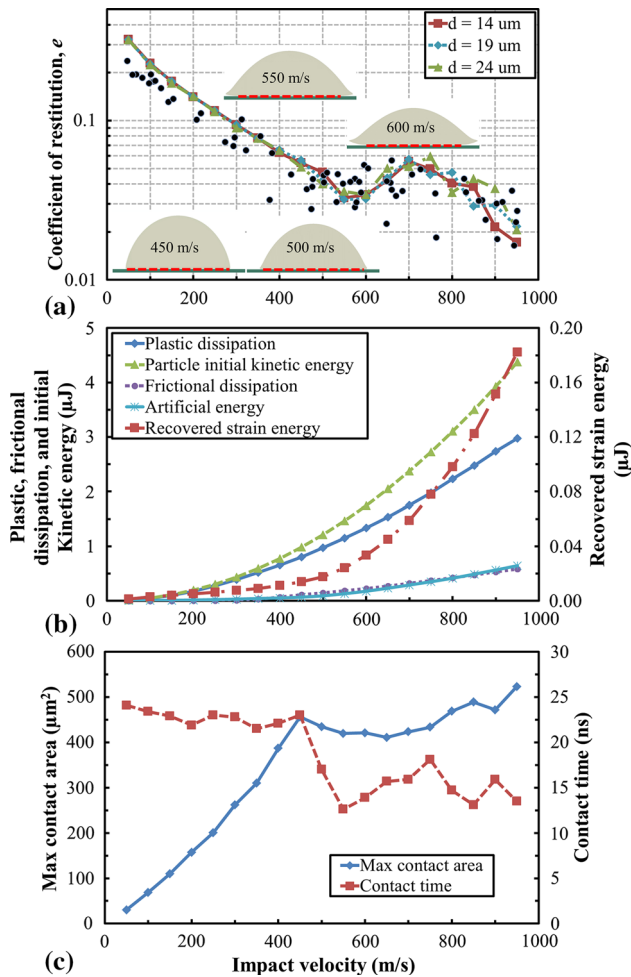


**Fig. 5** (a) Coefficient of restitution as a function of impact velocity from both experimental and simulation results. Deformed particle morphologies at the moment of maximum contact for four cases are included. The red dashed lines indicate the contact interface. (b) Evolution of energy components in the system with respect to impact velocity. (c) Evolution of maximum contact area and contact duration with respect to impact velocity

size for 14–25  $\mu\text{m}$  within the velocity range of 200–800 m/s.

Close inspection of Fig. 5a also reveals three distinct regimes in the impact velocity ranges of 0–500 m/s, 500–850 m/s and 850–950 m/s. The plastic energy  $U_p$  increases nearly in proportion to the kinetic energy  $E_k$  of the particle in the relatively low impact velocity regime, until approximately 450 m/s (Fig. 5b). The maximum contact area  $A_c$  also increases similarly in the same velocity regime (Fig. 5c). However, very distinct changes in the variation of  $A_c$  and  $U_p$  occur near 450 and 500 m/s, respectively. Significant horizontal spreading and jetting of the particle is observed in the simulation and experiments for impact velocities greater than 500 m/s (Fig. 4 and inset of Fig. 5a). These figures show that the “jetted” regions of the particle are not in contact with the substrate when the

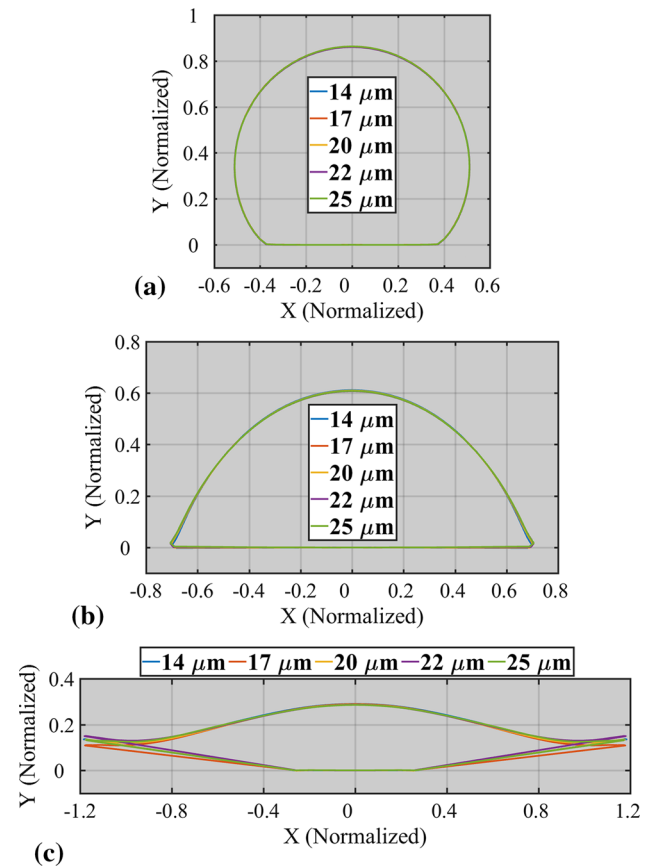


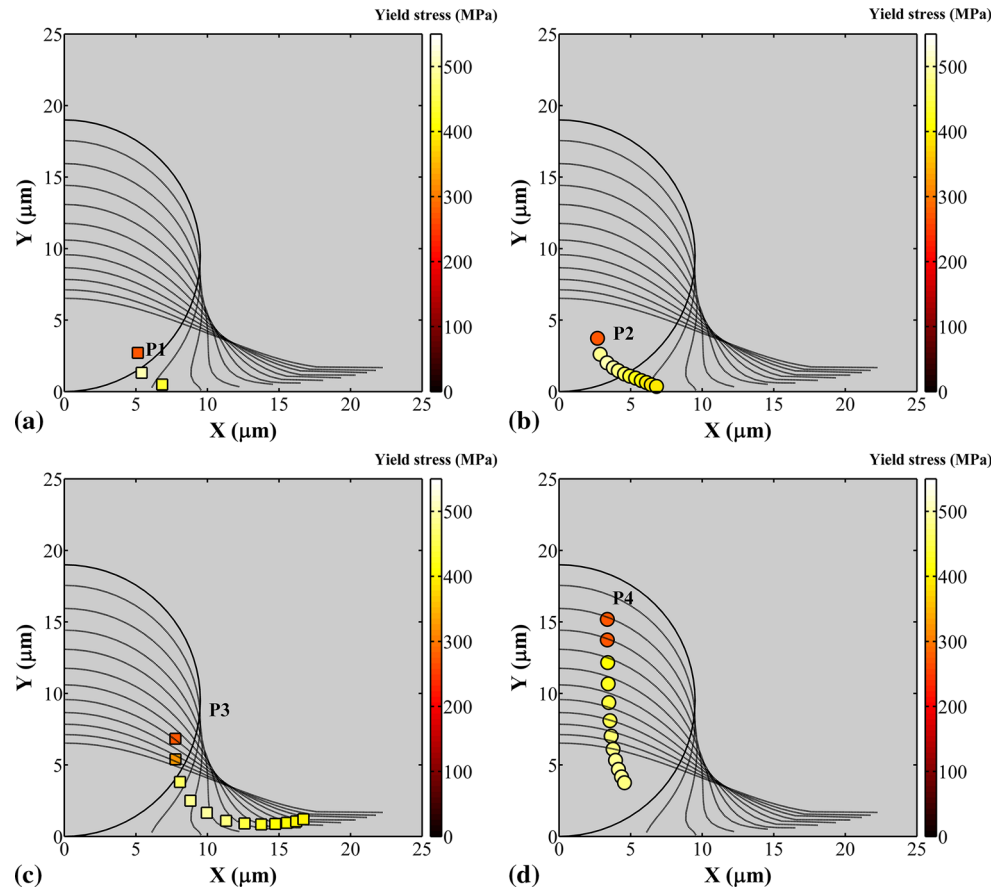
**Fig. 6** Effects of the original particle diameter (14–25  $\mu\text{m}$ ) on the post-impact shape of the particles. Profiles are normalized with respect to original particle diameters. (a) 200 m/s, (b) 500 m/s, (c) 800 m/s

contact area is at its maximum; therefore, the contact radius and hence contact area do not change significantly with further increase in impact velocity. The recovered elastic strain energy of the system begins to increase sharply near the same transition point, and thus the coefficient of restitution experiences the first transition observed in Fig. 5a. Note that the frictional energy dissipation in the contact interface has a minor role in this process.

The abrupt change in the plastic dissipation and the observed spreading beyond  $v_i = 500$  m/s is indicative of a transition of the flow behavior of the material. This can be observed clearly by following the deformation path and material properties of the material points of the particle during impact. Figure 7 shows the deformation and flow stress histories of four points with 2-ns intervals for a particle impacting with 800 m/s. All of the material points are initially internal and belong to different regions identified later in the paper.

As the particle deforms, all four material points are displaced toward the substrate. Point P1 experiences greatest amount of damage ( $\varepsilon_p > 3$ ) and is removed from

**Fig. 7** Temporal evolution of the particle profile with intervals of 2 ns. The impact velocity of 800 m/s is along the negative Y direction. Each marker represents the material point's location at a different time, whereas its color indicates the contemporary yield stress. (a) Point P1, (b) point P2, (c) point P3, (d) point P4



analysis within 8 ns. Points P2 and P3, which are initially internal to the particle, experience excessive amount of shear, where P2 finishes by contacting the substrate and P3 ends up near the tip of the jet region. Note that all three material points experience an initial increase in their flow stress followed by a noticeable drop. The material point P4, which was initially farthest from the substrate, experiences the least amount of displacement relative to the particle, but nevertheless it too experiences substantial increase in the flow stress.

The equivalent plastic strain  $\varepsilon_p$ , strain rate  $\dot{\varepsilon}_p$ , temperature  $T$  and the flow stress  $\sigma_Y$  of all the material points (i.e., mesh points in the analysis) were monitored as functions of impact duration and impact velocity (50–950 m/s). Note that rebound typically occurs within 30 ns after impact. Therefore, only the first 30 ns is shown in the following plots. These variables were investigated in terms of their effects on the flow stress according to Eq 1. Therefore, the strain hardening term  $(1 + B/A\varepsilon_p^n)$ , the strain-rate hardening term  $(1 + C \ln \dot{\varepsilon}_p/\dot{\varepsilon}_0)$  and the temperature dependence term  $(1 - T^{*m})$ , with  $T^* = (T - T_R)/(T_m - T_R)$ , are plotted in Fig. 8–10, respectively.

For all four points, accumulation of plastic strain  $\varepsilon_p$  is relatively low for impact velocities that are slower than

200 m/s. For P1, the plastic strain rises to a value around  $\varepsilon_p = 2.5$  (or  $1 + B/A\varepsilon_p^n = 1.71$ ) when impact velocity is  $v_i \sim 470$  m/s and stays almost constant thereafter. With increasing impact velocity, the plastic strain accumulates to 3 ( $1 + B/A\varepsilon_p^n = 1.74$ ) quickly and the material point (P1) is considered failed and eliminated from the calculation. This phenomenon is predicted for P2 around an impact velocity of 800 m/s. It is seen in Fig. 11 that between 500 m/s and 950 m/s of impact velocity, a little over 10% of the material experiences failure due to material instability. No material failure is predicted for P3 and P4. The number of elements removed due to material instability introduces an increasing uncertainty to the predicted results with increasing impact velocity. The effects of this should be addressed in future work.

In general, the temperature rise  $(T - T_R)$  in all four investigated points ranges from 0–300 deg. C. Note that an increase in  $T$  is reflected as a decrease in the variable  $(1 - T^{*m})$ , and the range 0–300 deg. C corresponds to 1–0.65 in terms of this variable. The material points P1 and P2 experience faster temperature rise than P3 and P4 due to rapid accumulation of plastic strain. As 90% of the plastic strain energy  $U_p$  is converted to heat, material temperature



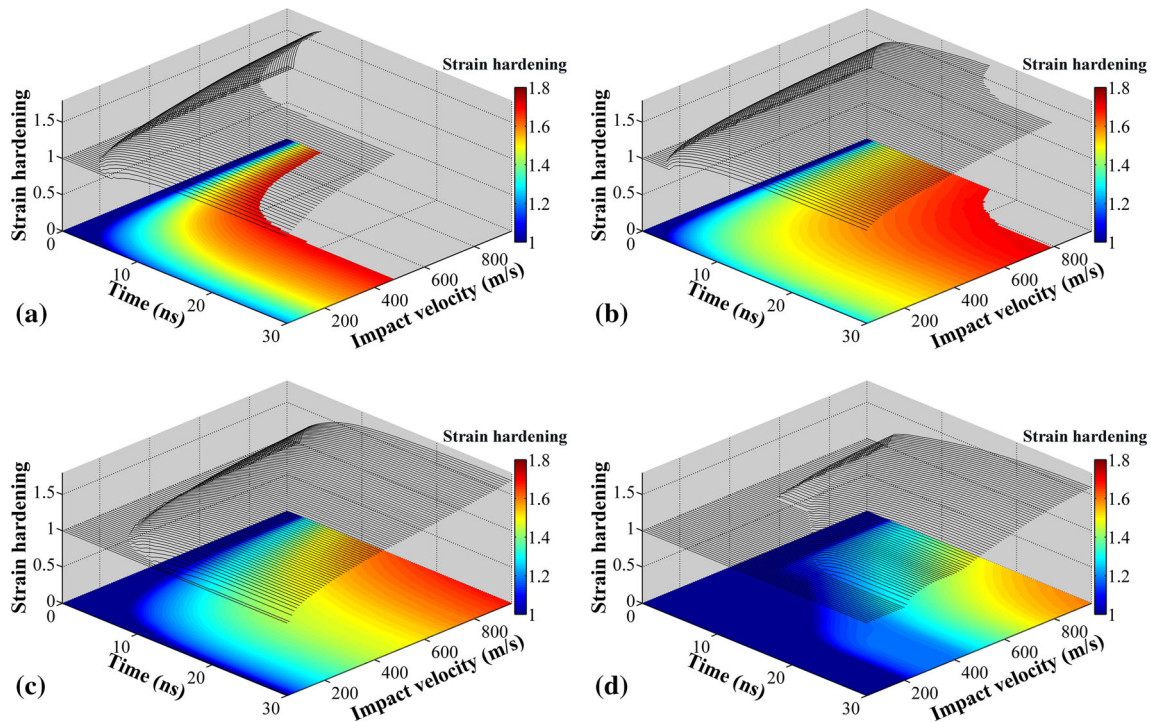


**Fig. 8** Normalized value of strain hardening term in JC model of each point as a function of time and velocity, shown as line and contour plots where blank area in the contour plots signifies that this

material point belongs to an extremely distorted element and has therefore been removed from simulation. (a) Point P1, (b) point P2, (c) point P3, (d) point P4

risks 300 deg. C above room temperature within the first few nanoseconds following the impact. This effect gets worse for the particle at higher impact speeds. Points P3 and P4 experience this effect too, but as the plastic strain is not as drastically increased at these points, the precipitous drop of the softening term is not predicted.

The strain rates of points P1 and P2 rise to the order of  $10^9 \text{ s}^{-1}$ , within the first 5 ns following the initiation of contact. The strain rates of  $10^9$ ,  $10^8$  and  $10^7$  correspond to  $(1 + C \ln \dot{\epsilon}_p / \dot{\epsilon}_0) = 1.43, 1.36$  and  $1.29$ , respectively. The peak strain rates of P3 and P4 are much less prominent when plotted in the same scale as P1.

The flow stress depends on highly coupled phenomena related to strain and strain-rate hardening, and thermal softening. The plastic strain  $\epsilon_p$  increases very rapidly due to the high strain rate  $\dot{\epsilon}_p$  at P1 and P2 for  $v_i$  values faster than 500 and 800 m/s, respectively. This results in rapid increase in local temperature. On the other hand, the local flow stress  $\sigma_Y$  displays a rapid increase followed by a rapid drop. For example, at P1, Fig. 8a, 9a, 10a and 12a show that the strain and strain-rate hardening effects are not attenuating when the drop in yield stress is observed, while the value of the thermal softening term is rapidly decreasing. It is therefore reasonable to state that the

thermal softening effect is outweighing the strain and strain-rate hardening effects, and a *material instability* develops at this material point. While the flow stress drop dominated by thermal softening is also observed at material points P2, P3 and P4, its effect on the flow stress is lower.

The particle can be demarcated into four characteristic regions of material behavior as shown in Fig. 13. All of the material points in the regions marked 1-4, from which the analyzed points were selected, behave in a very similar way to points P1-P4 in terms of flow stress development. That is, the material instability is anticipated in region-1 and region-2 for impact velocities faster than  $\sim 500 \text{ m/s}$  and  $\sim 800 \text{ m/s}$ , respectively, while in region-3 and region-4 this phenomenon is not predicted. In region-3, which encircles region-2, yield stress drop caused by thermal softening is observed as well; however, the rate of such drop is much lower when compared to those in region-1 and region-2. In the rest of the particle, which lies beyond region-3, the trend of flow stress of material closely resembles the pattern of strain rate term in JC plasticity model. Finally, the horizontal spreading and jetting of the particle observed in the experiments above 500 m/s in Fig. 4 and 5 are attributed to the occurrence of material instability in region-1 and region-2.

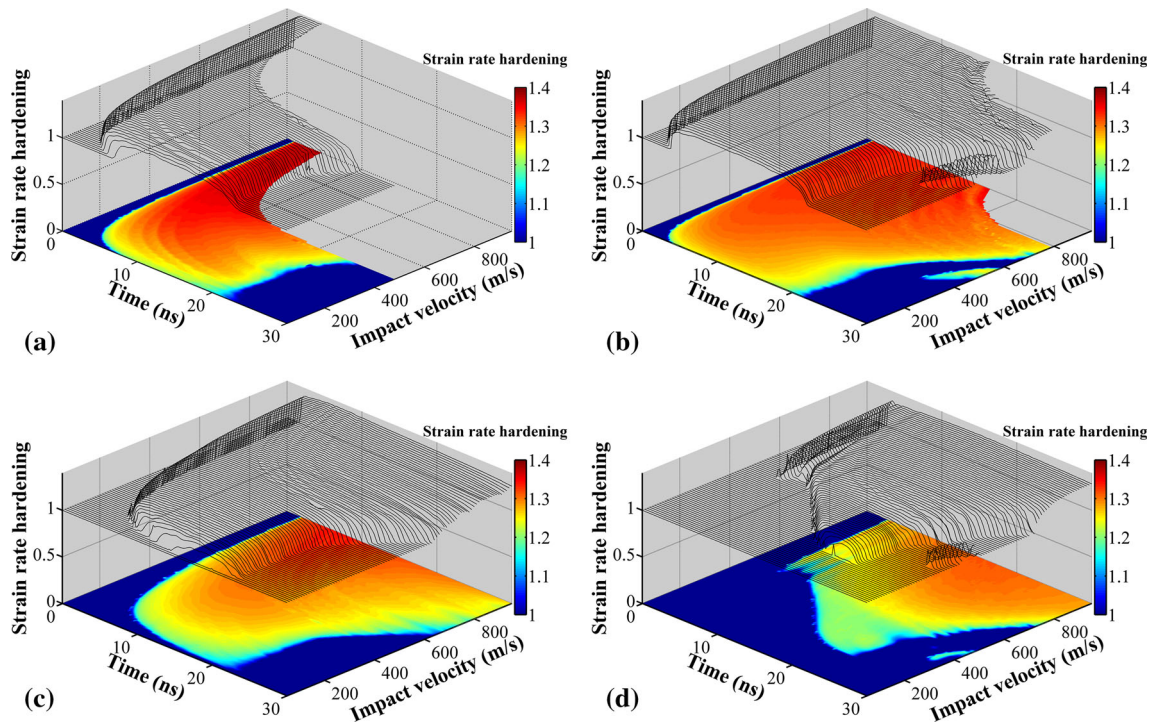


**Fig. 9** Value of strain-rate hardening term in JC model of each point as a function of time and velocity, shown as line and contour plots where blank area in the contour plots signifies that this material point

belongs to an extremely distorted element and has therefore been removed from simulation. (a) Point P1, (b) point P2, (c) point P3, (d) point P4

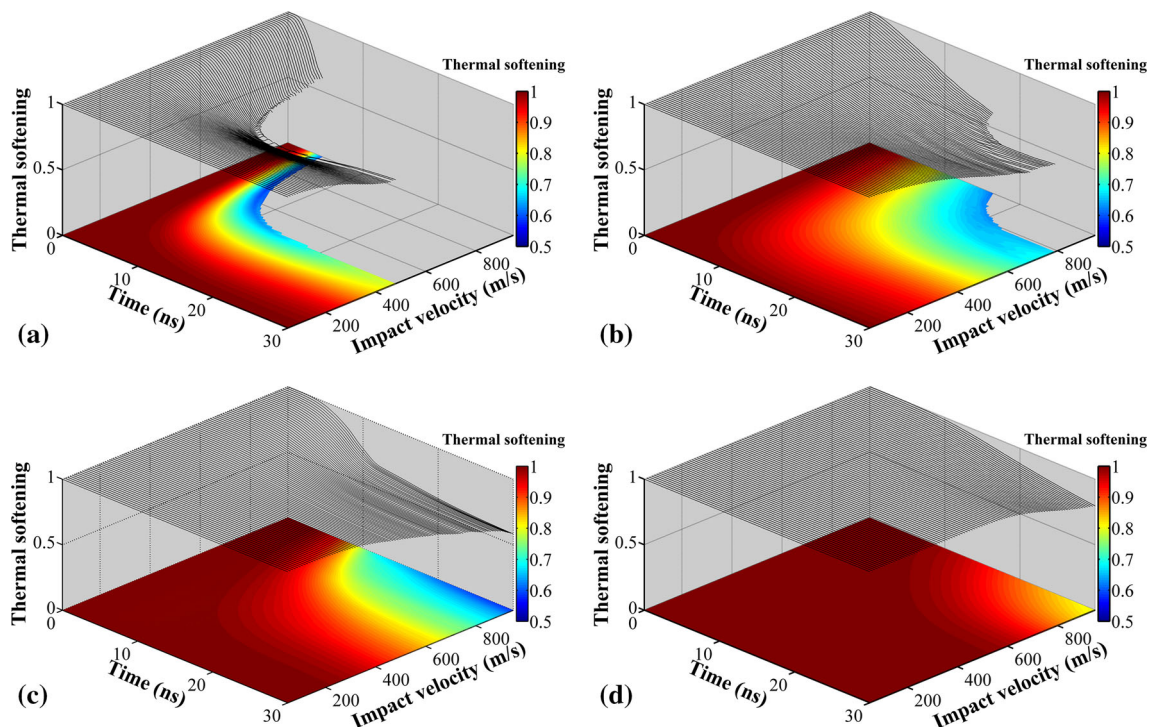


**Fig. 10** Value of thermal softening term in JC model of each point as a function of time and velocity, shown as line and contour plots where blank area in the contour plots signifies that this material point

belongs to an extremely distorted element and has therefore been removed from simulation. (a) Point P1, (b) point P2, (c) point P3, (d) point P4



## Summary and Conclusions

In this work, a bilinear JC plasticity model for Al-6061 was introduced based on the results of impact experiments of micron-scale spherical particles with a sapphire surface.

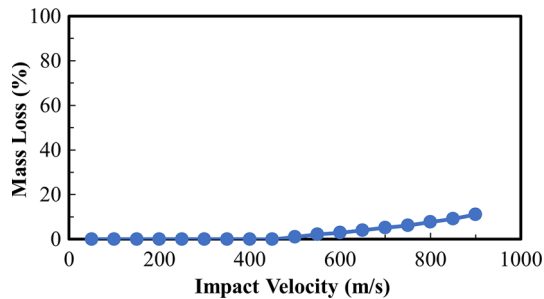


**Fig. 11** Mass loss due to element deletion as a function of impact velocity. Mass loss due to element deletion starts at the velocity of 500 m/s and reaches its maximum around 12% of original mass at the highest velocity, i.e., 900 m/s. The location of the elements that were removed is shown in Fig. 13. In region-1, element deletion was observed at impact velocities as low as 500 m/s, while in region-2, element deletion is observed only at velocities higher than 500 m/s

*Laser-induced projectile impact test* (LIPIT) was used to test impact of individual spherical particles (14–25  $\mu\text{m}$ ) in the velocity range of 50–950 m/s. A modified version of the steepest descent method was employed to find the material parameters of the JC plasticity model based on comparison of deformed and computed particle shapes. The increases in the plastic and frictional dissipation energies with impact velocity were found to be inherently lower than the increase in the kinetic energy. This was found to lead to instability and an evident transition in the rebound behavior when the impact velocity is  $\sim 500$  m/s. Distinct material behaviors were identified at four different locations inside the particle by analyzing the temporal variation of the variables that contribute to the flow stress of the particle. In a small region of the particle, dramatic yield stress drop due to thermal softening is spotted; this is the material instability. As a result, the local load carrying capacity of the material degrades drastically and leads to the rapid horizontal expanding and jetting of the particle for impact velocities greater than 500 m/s.

Impact investigated in this work is expected to be more severe than a typical CS application due to the rigidity of

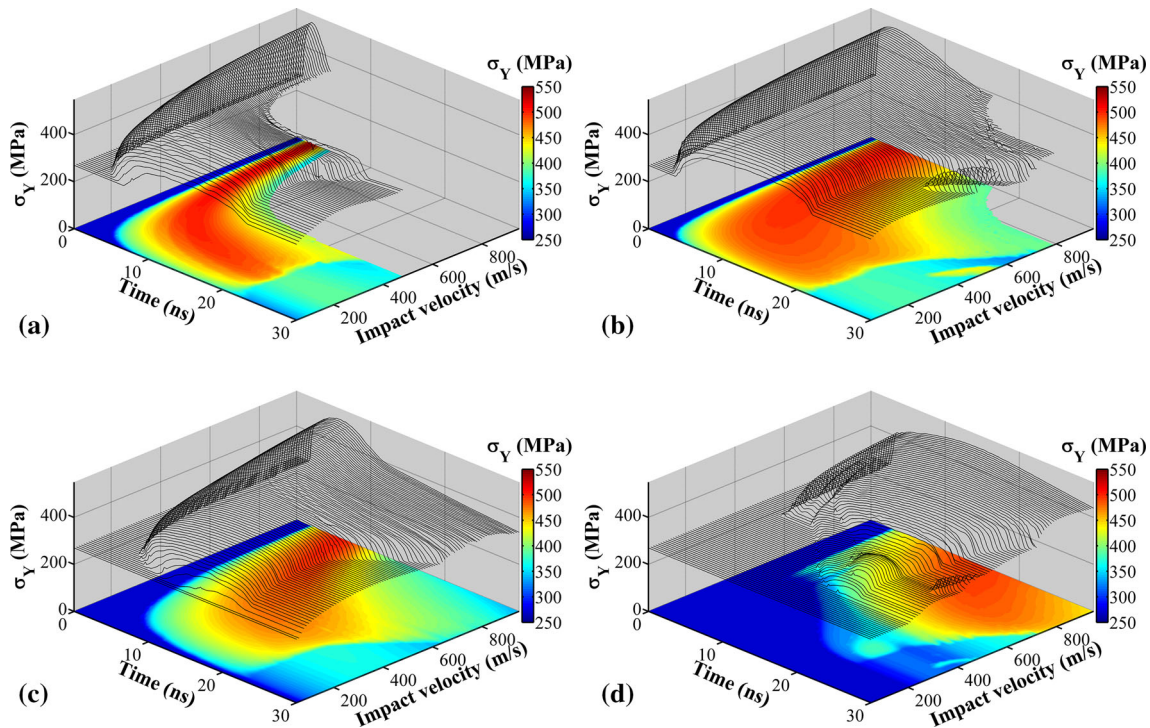
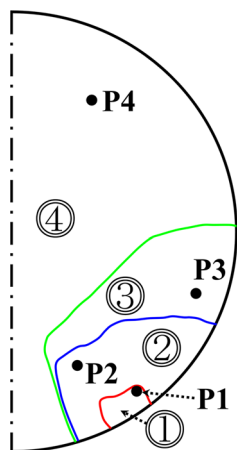


**Fig. 12** Flow stress of each point as a function of time and velocity, shown as line and contour plots where blank area in the contour plots signifies that this material point belongs to an extremely distorted

element and has therefore been removed from simulation. (a) Point P1, (b) point P2, (c) point P3, (d) point P4

**Fig. 13** The four material points (P1-P4) were chosen from the four regions of the particle that experience different levels of damage and flow stress behavior



the substrate. To provide accurate predictions for aluminum on aluminum or other identical material impacts, experiments with softer substrates should be conducted. Nevertheless, this work advances the knowledge on material instability at high strain rates and is expected to be a useful guide for interpretation of future experimental and theoretical studies.

## References

1. S.V. Klinkov, V.F. Kosarev, and M. Rein, Cold Spray Deposition: Significance of Particle Impact Phenomena, *Aerosp. Sci. Technol.*, 2005, **9**(7), p 582-591
2. M.A. Meyers, *Dynamic Behavior of Materials*, Wiley, New York, 1994
3. G.T. Gray, *Classic Split-Hopkinson Pressure Bar Testing*, ASM International, Materials Park, OH, 2000, p 462-476
4. H. Kolsky, An Investigation of the Mechanical Properties of Materials at Very High Rates of Loading, *Proc. Phys. Soc. Lond. B*, 1949, **62**(11), p 676
5. J. Harding, E. Wood, and J. Campbell, Tensile Testing of Materials at Impact Rates of Strain, *J. Mech. Eng. Sci.*, 1960, **2**(2), p 88-96
6. F.E. Hauser, Techniques for Measuring Stress-Strain Relations at High Strain Rates, *Exp. Mech.*, 1966, **6**(8), p 395-402
7. U. Lindholm and L. Yeakley, High Strain-Rate Testing: Tension and Compression, *Exp. Mech.*, 1968, **8**(1), p 1-9
8. D. Rittel, S. Lee, and G. Ravichandran, A Shear-Compression Specimen for Large Strain Testing, *Exp. Mech.*, 2002, **42**(1), p 58-64
9. J. Zhao, H. Li, and Y. Zhao, *Dynamic Strength Tests of the Bukit Timah Granite*, Nanyang Technological University, Singapore, 1998
10. S. Huang, X. Feng, and K. Xia, A Dynamic Punch Method to Quantify the Dynamic Shear Strength of Brittle Solids, *Rev. Sci. Instrum.*, 2011, **82**(5), p 053901
11. J. Zhao, *An Overview of Some Recent Progress in Rock Dynamics Research*, Advances in Rock Dynamics and Applications. CRC Press, Boca Raton, 2011, p 5-33
12. R. Armstrong and F. Zerilli, Dislocation Mechanics Aspects of Plastic Instability and Shear Banding, *Mech. Mater.*, 1994, **17**(2-3), p 319-327
13. C. Gao and L. Zhang, Constitutive Modelling of Plasticity of FCC Metals Under Extremely High Strain Rates, *Int. J. Plast.*, 2012, **32**, p 121-133
14. G.R. Johnson, and W.H. Cook, A Constitutive Model and Data for Metals Subjected to Large Strains, High Strain Rates and High Temperatures, *Proceedings of the 7th International Symposium on Ballistics*, The Hague, The Netherlands, 1983
15. A.S. Khan and R. Liang, Behaviors of Three BCC Metal Over a Wide Range of Strain Rates and Temperatures: Experiments and Modeling, *Int. J. Plast.*, 1999, **15**(10), p 1089-1109
16. A.S. Khan and R. Liang, Behaviors of Three BCC Metals During Non-proportional Multi-axial Loadings: Experiments and Modeling, *Int. J. Plast.*, 2000, **16**(12), p 1443-1458
17. D.L. Preston, D.L. Tonks, and D.C. Wallace, Model of Plastic Deformation for Extreme Loading Conditions, *J. Appl. Phys.*, 2003, **93**(1), p 211-220
18. G.Z. Voyiadjis and F.H. Abed, Microstructural Based Models for BCC and FCC Metals with Temperature and Strain Rate Dependency, *Mech. Mater.*, 2005, **37**(2), p 355-378
19. M. Grujicic, C. Zhao, W. DeRosset, and D. Helfrich, Adiabatic Shear Instability Based Mechanism for Particles/Substrate Bonding in the Cold-Gas Dynamic-Spray Process, *Mater. Des.*, 2004, **25**(8), p 681-688
20. T. Hu, S. Zhalehpour, A. Gouldstone, S. Muftu, and T. Ando, A Method for the Estimation of the Interface Temperature in Ultrasonic Joining, *Metall. Mater. Trans. A*, 2014, **45**(5), p 2545-2552
21. V.K. Champagne, Jr., D. Helfrich, P. Leyman, S. Grendahl, and B. Klotz, Interface Material Mixing Formed by the Deposition of Copper on Aluminum by Means of the Cold Spray Process, *J. Therm. Spray Technol.*, 2005, **14**(3), p 330-334
22. M. Grujicic, J. Saylor, D. Beasley, W. DeRosset, and D. Helfrich, Computational Analysis of the Interfacial Bonding Between Feed-Powder Particles and the Substrate in the Cold-Gas Dynamic-Spray Process, *Appl. Surf. Sci.*, 2003, **219**(3), p 211-227
23. S. Guetta, M.-H. Berger, F. Borit, V. Guipont, M. Jeandin, M. Boustie, Y. Ichikawa, K. Sakaguchi, and K. Ogawa, Influence of Particle Velocity on Adhesion of Cold-Sprayed Splats, *J. Therm. Spray Technol.*, 2009, **18**(3), p 331-342
24. T. Hussain, D. McCartney, P. Shipway, and D. Zhang, Bonding Mechanisms in Cold Spraying: The Contributions of Metallurgical and Mechanical Components, *J. Therm. Spray Technol.*, 2009, **18**(3), p 364-379
25. H. Assadi, F. Gärtner, T. Stoltenhoff, and H. Kreye, Bonding Mechanism in Cold Gas Spraying, *Acta Mater.*, 2003, **51**(15), p 4379-4394
26. W.-Y. Li, H. Liao, C.-J. Li, G. Li, C. Coddet, and X. Wang, On High Velocity Impact of Micro-sized Metallic Particles in Cold Spraying, *Appl. Surf. Sci.*, 2006, **253**(5), p 2852-2862
27. T. Schmidt, H. Assadi, F. Gärtner, H. Richter, T. Stoltenhoff, H. Kreye, and T. Klassen, From Particle Acceleration to Impact and Bonding in Cold Spraying, *J. Therm. Spray Technol.*, 2009, **18**(5-6), p 794
28. T. Schmidt, F. Gärtner, H. Assadi, and H. Kreye, Development of a Generalized Parameter Window for Cold Spray Deposition, *Acta Mater.*, 2006, **54**(3), p 729-742
29. W. Li, D. Zhang, C. Huang, S. Yin, M. Yu, F. Wang, and H. Liao, Modelling of Impact Behaviour of Cold Spray Particles: Review, *Surf. Eng.*, 2014, **30**(5), p 299-308
30. G. Bae, Y. Xiong, S. Kumar, K. Kang, and C. Lee, General Aspects of Interface Bonding in Kinetic Sprayed Coatings, *Acta Mater.*, 2008, **56**(17), p 4858-4868



31. B. Yildirim, H. Fukanuma, T. Ando, A. Gouldstone, and S. Müftü, A Numerical Investigation into Cold Spray Bonding Processes, *J. Tribol.*, 2015, **137**(1), p 011102
32. S. Müftü, S. Zhalehpour, A. Gouldstone, and T. Ando, Assessment of Interface Energy in High Velocity Particle Impacts, *38th Annual Meeting of The Adhesion Society*. Savannah, GA, 2015
33. B. Yildirim, S. Müftü, and A. Gouldstone, On Cohesion of Micron Scale Metal Particles in High Velocity Impact with a Metal Substrate, *ASME/STLE 2011 International Joint Tribology Conference*, American Society of Mechanical Engineers, 2011
34. W.-Y. Li, C. Zhang, X. Guo, C.-J. Li, H. Liao, and C. Coddet, Study on Impact Fusion at Particle Interfaces and Its Effect on Coating Microstructure in Cold Spraying, *Appl. Surf. Sci.*, 2007, **254**(2), p 517-526
35. A. Alkhimov, A. Gudilov, V. Kosarev, and N. Nesterovich, Specific Features of Microparticle Deformation Upon Impact on a Rigid Barrier, *J. Appl. Mech. Tech. Phys.*, 2000, **41**(1), p 188-192
36. G. Bae, S. Kumar, S. Yoon, K. Kang, H. Na, H.-J. Kim, and C. Lee, Bonding Features and Associated Mechanisms in Kinetic Sprayed Titanium Coatings, *Acta Mater.*, 2009, **57**(19), p 5654-5666
37. S. Schoenfeld and T. Wright, A Failure Criterion Based on Material Instability, *Int. J. Solids Struct.*, 2003, **40**(12), p 3021-3037
38. T.W. Wright and J.W. Walter, On Stress Collapse in Adiabatic Shear Bands, *J. Mech. Phys. Solids*, 1987, **35**(6), p 701-720
39. T. Wright and H. Ockendon, A Scaling Law for the Effect of Inertia on the Formation of Adiabatic Shear Bands, *Int. J. Plast.*, 1996, **12**(7), p 927-934
40. T. Wright, Shear Band Susceptibility: Work Hardening Materials, *Int. J. Plast.*, 1992, **8**(5), p 583-602
41. B. Yildirim, S. Müftü, and A. Gouldstone, Modeling of High Velocity Impact of Spherical Particles, *Wear*, 2011, **270**(9-10), p 703-713
42. W. Xie, A. Alizadeh-Dehkharghani, Q. Chen, V.K. Champagne, X. Wang, A.T. Nardi, S. Kooi, S. Müftü, and J.-H. Lee, Dynamics and Extreme Plasticity of Metallic Microparticles in Supersonic Collisions, *Sci. Rep.*, 2017, **7**, p 5073
43. J.-H. Lee, P.E. Loya, J. Lou, and E.L. Thomas, Dynamic Mechanical Behavior of Multilayer Graphene Via Supersonic Projectile Penetration, *Science*, 2014, **346**(6213), p 1092-1096
44. J.-H. Lee, D. Veyssset, J.P. Singer, M. Retsch, G. Saini, T. Pezeril, K.A. Nelson, and E.L. Thomas, High Strain Rate Deformation of Layered Nanocomposites, *Nature communications*, 2012, **3**, p 1164
45. S. Barradas, V. Guipont, R. Molins, M. Jeandin, M. Arrigoni, M. Boustie, C. Bolis, L. Berthe, and M. Ducos, Laser Shock Flier Impact Simulation of Particle-Substrate Interactions in Cold Spray, *J. Therm. Spray Technol.*, 2007, **16**(4), p 548-556
46. M. Arrigoni, M. Boustie, C. Bolis, S. Barradas, L. Berthe, and M. Jeandin, Shock Mechanics and Interfaces, *Mechanics of Solid Interfaces*, M. Braccini and M. Dupeux, Eds., John Wiley & Sons, Inc., Hoboken, NJ, USA, 2012. <https://doi.org/10.1002/9781118561669.ch7>
47. M. Jeandin, D.K. Christoulis, F. Borit, M.-H. Berger, S. Guetta, G. Rolland, V. Guipont, F. N'Guyen, D. Jeulin, and E. Irissou, A Socratic Approach to Surface Modification: The Example of Thermal Spray, *24th International Conference on Surface Modification Technologies, SMT 24*, 2010
48. M. Hassani-Gangaraj, D. Veyssset, K.A. Nelson, and C.A. Schuh, In-situ Observations of Single Micro-particle Impact Bonding, *Scripta Mater.*, 2018, **145**, p 9-13
49. Dassault Systèmes Simulia Corp., P., RI, USA, *ABAQUS/Explicit 6.13 User Manual*. 2013
50. Dehkharghani, A.A., Tuning Johnson-Cook Material Model Parameters for Impact of High Velocity, Micron Scale Aluminum Particles, *Department of Mechanical and Industrial Engineering*. 2016, MS Thesis, Northeastern University.
51. Yildirim, B., *Mechanistic Modeling of High Velocity Micro-particle Impacts: Application to Material Deposition by Cold Spray Process*, in *Department of Mechanical and Industrial Engineering*. 2013, PhD Thesis, Northeastern University
52. T. Belytschko, J.S.-J. Ong, W.K. Liu, and J.M. Kennedy, Hourglass Control in Linear and Nonlinear Problems, *Comput. Methods Appl. Mech. Eng.*, 1984, **43**(3), p 251-276
53. JAHM Software Inc., I., *MPDB Material Database Software*, 1998
54. A. Manes, D. Lumassi, L. Giudici, and M. Giglio, An Experimental-Numerical Investigation on Aluminium Tubes Subjected to Ballistic Impact with Soft Core 7.62 Ball Projectiles, *Thin-Walled Structures*, 2013, **73**, p 68-80
55. A. Manes, L. Peroni, M. Scapin, and M. Giglio, Analysis of Strain Rate Behavior of an Al 6061 T6 Alloy, *Procedia Engineering*, 2011, **10**, p 3477-3482
56. R.G. Munro, Evaluated Material Properties for a Sintered alpha-Alumina, *J. Am. Ceram. Soc.*, 1997, **80**(8), p 1919-1928
57. S.P. Keeler and W.A. Backofen, Plastic Instability and Fracture in Sheets Stretched Over Rigid Punches, *Asm. Trans. Q.*, 1963, **56**(1), p 25-48
58. Z. Marciniak and K. Kuczyński, Limit Strains in the Processes of Stretch-Forming Sheet Metal, *Int. J. Mech. Sci.*, 1967, **9**(9), p 609IN1613-612IN2620
59. G.R. Johnson and W.H. Cook, Fracture Characteristics of Three Metals Subjected to Various Strains, Strain Rates, Temperatures and Pressures, *Eng. Fract. Mech.*, 1985, **21**(1), p 31-48
60. F.J. Zerilli and R.W. Armstrong, Dislocation-Mechanics-Based Constitutive Relations for Material Dynamics Calculations, *J. Appl. Phys.*, 1987, **61**(5), p 1816-1825
61. R. Liang and A.S. Khan, A Critical Review of Experimental Results and Constitutive Models for BCC and FCC Metals Over a Wide Range of Strain Rates and Temperatures, *Int. J. Plast.*, 1999, **15**(9), p 963-980
62. S. Rahmati and A. Ghaei, The Use of Particle/Substrate Material Models in Simulation of Cold-Gas Dynamic-Spray Process, *J. Therm. Spray Technol.*, 2014, **23**(3), p 530-540
63. D.R. Lesuer, G. Kay, and M. LeBlanc, Modeling Large-Strain, High-Rate Deformation in Metals, *Third Biennial Tri-Laboratory Engineering Conference on Modeling and Simulation*, Lawrence Livermore National Laboratory: Pleasanton, CA (US), 2001
64. L. Pun, *Introduction to Optimization Practice*, Wiley, New York, 1969
65. L.R. Grace and M. Altan, Characterization of Anisotropic Moisture Absorption in Polymeric Composites Using Hindered Diffusion Model, *Compos. A Appl. Sci. Manuf.*, 2012, **43**(8), p 1187-1196
66. K.L. Johnson, *Contact Mechanics*, Cambridge University Press, Cambridge Cambridgeshire; New York, 1985, p 452
67. B. Yildirim, H. Yang, A. Gouldstone, and S. Müftü, Rebound Mechanics of Micrometre-Scale, Spherical Particles in High-Velocity Impacts, *Proc. R. Soc. A.*, 2017, **473**, p 20160936